The *VOLMAX* Transient Electromagnetic Modeling System, Including Sub-Cell Slots and Wires on Random Non-Orthogonal Cells

Douglas J. Riley and C. David Turner

Radiation and Electromagnetic Analysis Department
Sandia National Laboratories, Albuquerque New Mexico 87185-1166
Internet: djriley@sandia.gov

1. Introduction

VOLMAX is a three-dimensional transient *vol*umetric *Max*well equation solver that operates on standard rectilinear finite-difference time-domain (FDTD) grids, non-orthogonal unstructured grids, or a combination of both types (hybrid grids) [1-3]. The algorithm is fully explicit. Open geometries are typically solved by embedding multiple unstructured regions into a simple rectilinear FDTD mesh. The grid types are fully connected at the mesh interfaces without the need for complex spatial interpolation. The approach permits detailed modeling of complex geometry while mitigating the large cell count typical of non-orthogonal cells such as tetrahedral elements. To further improve efficiency, the unstructured region carries a separate time step that sub-cycles relative to the time-step used in the FDTD mesh. A cross section of the interface between finite-volume time-domain (FVTD) and FDTD grids is shown in Fig. 1. The "wrapper layer" is a hexahedral region that encloses the unstructured grid and provides nodal connectivity to the surrounding FDTD mesh. The wrapper is constructed automatically based on the unstructured-grid topology. The unstructured region may consist of a single rectangular block, or be of a multiple, block-on-block form.

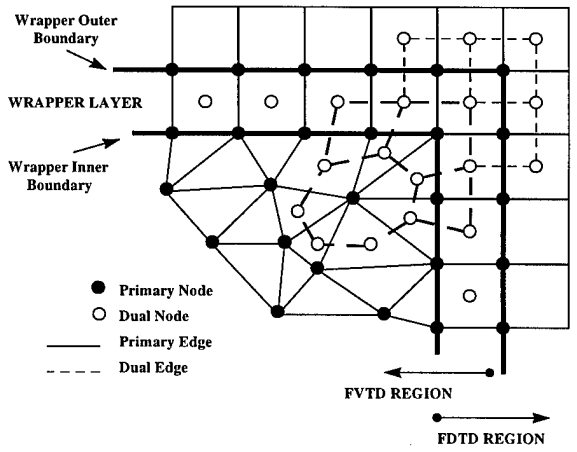

Fig. 1. The hybrid grid interface.

As shown in Fig. 1, *VOLMAX* is based on a staggered grid formulation. Primary and dual grids are used. When the unstructured grid consists exclusively of rectangular hexahedral cells, the field advancement is identically FDTD in nature, although the cells are referenced in an unstructured (indirect) manner. Note that the wrapper layer consists of rectangular cells for it's primary grid, but the dual cells on the wrapper inner boundary are generally non-orthogonal. As a consequence, the wrapper layer is common to both the FVTD and FDTD grids. For the case that the unstructured-grid consists of rectangular elements, the algorithm is second-order accurate both in space and time.

The field advancement scheme for the *VOLMAX* hybrid mesh is the following. The electric fields in the FDTD region are initially advanced based on time step, Δt_s. On the outer boundary of the wrapper, the tangential electric fields are second-order time interpolated to provide a Dirichlet boundary condition for the FVTD region. The electric and magnetic fields in the FVTD region are advanced an integral number of sub-time iterations relative to Δt_s. At the completion of the sub-cycling, the tangential electric fields on the inner boundary of the wrapper are used to provide a Dirichlet boundary condition to complete the magnetic-field advancement in the FDTD region. An alternative scheme could map the magnetic fields in the wrapper layer into the respective FDTD locations after the FDTD magnetic fields are advanced in time.

VOLMAX is currently integrated to the commercial CAD package SDRC I-DEAS [4]. Solid model design, mesh generation, and post processing are all accomplished through the I-DEAS interface. Electromagnetic properties, such as voltage sources, local boundary conditions, current observers, input and output ports, slots, wires, etc., are implemented by assigning nodal attributes to the desired property. The original I-DEAS grid file is input into the *VOLMAX* preprocessor, *PreVol*, which builds the wrapper layer, and the primary and dual grids. Grid construction by *PreVol* is accomplished at the rate of 50,000 to 100,000 cells/minute on a single, high-end processor. Construction time scales

DISCLAIMER

linearly with cell count. The basic user interface for *PreVol* in shown in Fig. 2. Typical inputs include the simulation domain (interior/exterior), node attributes (sources, observers, etc.), and (optionally) the topology of the unstructured region(s).

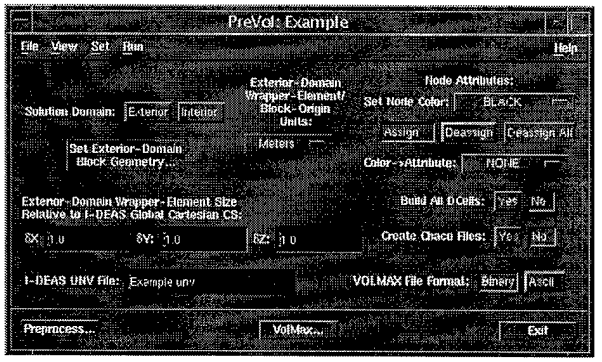

Fig. 2. The basic *PreVol* interface.

The overall design and simulation procedure used in the *VOLMAX* system is outlined in Fig. 3. The closed loop permits an adaptive cycle based on simulation results.

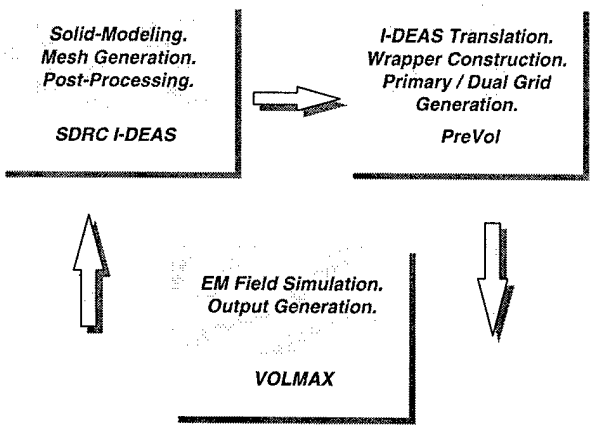

Fig. 3. The simulation cycle.

For demonstration purposes, application of *VOLMAX* is made to a cylindrical resonator and scattering by a simple conducting sphere in Section 2 of the paper. In Section 3, two methods for modeling sub-cell wires on arbitrary non-orthogonal cells are introduced. In Section 4, a generalization of the hybrid thin-slot algorithm (HTSA [5]) to arbitrary cell types is also introduced. EMC/EMI applications are made in Section 5. Concluding remarks are made in Section 6.

2. Application to Canonical Geometries

The hybrid-grid, far back-scattered field from a 0.5 m radius, perfectly conducting sphere gridded with tetrahedra and embedded in FDTD hexahedra is shown in Fig. 4. Note the good agreement with the Mie-series solution even as the resolution of the external FDTD mesh falls below 10 cells / wavelength (λ). A contour rendering of the surface current-density shortly after a Gaussian pulse has hit the sphere is shown in Fig. 5.

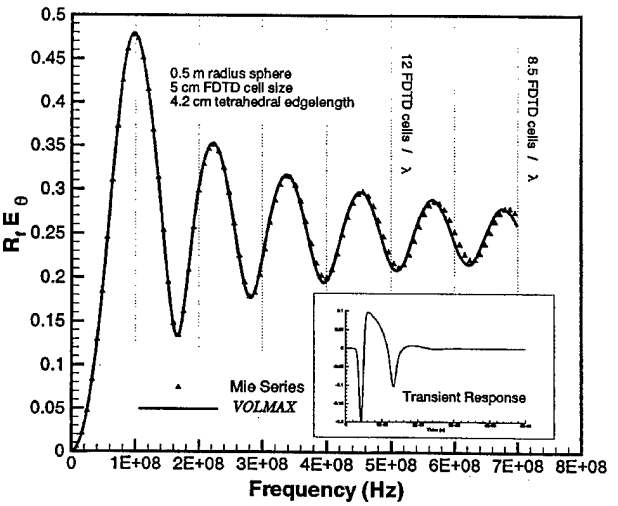

Fig. 4. The far, back-scattered field from a 0.5 m conducting sphere. R_f denotes distance. Hybrid-grid solution. The transient response is inset.

Fig. 5. The early time surface current density on a conducting sphere.

An extruded hexahedral element mesh for a simple cylindrical resonator is shown in Fig. 6. Random edges were selected for the source and observer. A Gaussian pulse excitation was used. The internal transient response demonstrating stability is shown in Fig. 7. The first few TM resonances are shown in Table 1.

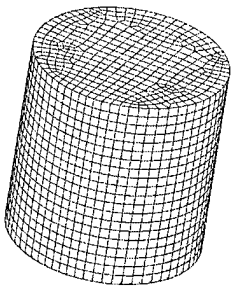

Fig. 6. Cylindrical resonator with an average hexahedral edgelength of 5 cm. The radius is 0.5 m and the height is 1 m.

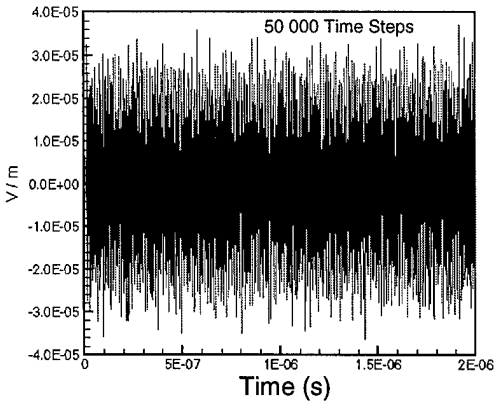

Fig. 7. Internal electric field after 50,000 time steps.

TABLE 1. Resonances of Cylindrical Resonator

Mode	Theory (MHz)	VOLMAX (MHz)
TM011	274.12	274.01
TM012	377.56	376.48
TM111	395.21	393.93
TM112	472.86	471.35
TM013	504.87	500.95

3. Sub-Cell Wire Modeling

The ability to model features that are small relative to the global cell size is important in electromagnetic simulations. By tapering an unstructured mesh, it is possible to resolve small detail; however, the increase in cell count and the reduction in time step can be prohibitive.

Relatively simple algorithms to resolve small wires on rectangular FDTD grids have been developed [6,7]. The algorithms are accurate but require that the wire conforms to the rectangular mesh. This can create problems for applications such as cellular phones that may demand the phone model to be tilted relative to the human head model.

Two algorithms are briefly presented here that enable wires to run arbitrarily along edges of an unstructured mesh. The first method embeds a transient integral equation into the unstructured mesh, whereas the second method is a generalization of the original FDTD scheme to non-orthogonal cells. A similar extension of the FDTD scheme was presented in [8], but the method was only applied to linear wires on prismatic cells. The technique in the present paper further extends and applies the method to curved wires on tetrahedral meshes.

3.1 Integral Equation Thin-Wire Model

A transient integral equation (IE) is used to model the topology of the wire. The wire is defined in the original solid model and is meshed using one-dimensional beam elements. Within *VOLMAX*, the IE operates in one of two modes. The first mode is an exclusive wire mode that is coupled to a *free-space* volumetric mesh. In this mode, *VOLMAX* is similar to a transient version of the frequency-domain *NEC* [9] code, with the added benefit of field visualization into the volumetric region. In the second mode, the IE operates in a field-feedback configuration that enables solid geometry to reside in the unstructured mesh. This algorithm is similar to the hybrid thin-slot algorithm [5] in that local vector fields computed in the volumetric region are injected back into the IE at each time step. These fields correspond to reflections from non-wire geometry and represent additional sources driving the IE. The field-feedback mode has been found to be most effective on hexahedral cells (that may be embedded in tetrahedral elements) and for wire radii that are a small fraction of the surrounding edge lengths that support the wire.

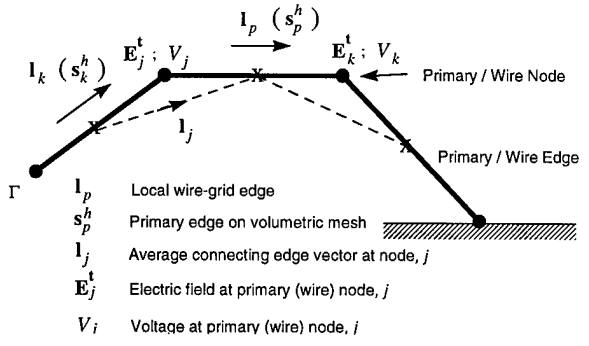

Fig. 8. Relationship of local wire-grid to volumetric primary mesh. Dual cells (not shown) enclose primary nodes.

A section of a simple curved wire is shown in Fig. 8. The IE solution uses overlapping piecewise-linear basis functions that are centered at the nodal positions. Only the governing equations are presented here. Numerical solution details for the IE are similar to Refs. [10,11].

The governing integral equation for the wire system, including the provision for volumetric-mesh feedback, is the following [cf. [11] for the $\nu = 0$ case].

$$\varepsilon_o \mathbf{l} \cdot \frac{\partial}{\partial t}\left(\mathbf{E}^{inc} + \nu \mathbf{E}^{\mathbf{t}}\right) =$$

$$\frac{1}{c^2}\frac{\partial^2}{\partial t^2}\int_{\Gamma} dl' \, \mathbf{l}\cdot\mathbf{l}' \, I\left(l',\tau\right)\left[G\left(\mathbf{r},\mathbf{r}';a\right) - \nu G\left(\mathbf{r},\mathbf{r}';a_o\right)\right] -$$

$$\mathbf{l}\cdot\nabla\int_{\Gamma} dl' \, \nabla_{l'}' \cdot \left[\mathbf{l}' \, I\left(l',\tau\right)\right]\left[G\left(\mathbf{r},\mathbf{r}';a\right) - \nu G\left(\mathbf{r},\mathbf{r}';a_o\right)\right] \quad (1)$$

where $\mathbf{r} \in \Gamma$, $\tau = t - \left|\mathbf{r}\text{-}\mathbf{r}'\right|/c$, c denotes the speed of light in vacuum, I denotes the current on the wire, $\mathbf{E}^{inc}$ denotes an impressed source on the wire, $\mathbf{E}^{\mathbf{t}}$ denotes the average total vector field from the volumetric grid local to the wire, $\nu = 0$ sets the equation to operate in a free-space (no feedback) mode, and $\nu = 1$ sets the equation to operate in a feedback mode from the volumetric grid. The free-space Green's function is denoted by $G()$ [11], a denotes the wire radius, and a_o denotes an effective radius for matching the integral equation solution to the volumetric solution local to the wire. Note that the volumetric solution for the electric field on the wire will not be identically zero because the solution represents an average value for the electric field over the dual cell containing the wire node; consequently, a_o is typically taken to be ½ the local dual-cell diameter.

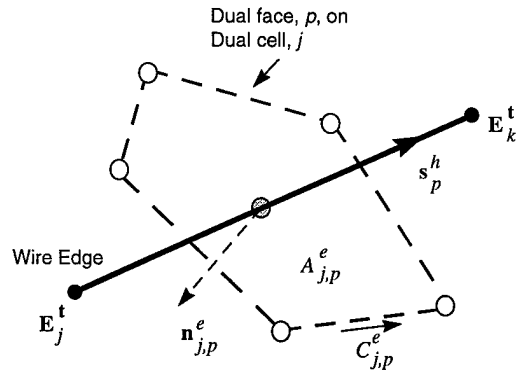

Fig. 9. Wire edge piercing dual face.

The integral equation solves for the current at the wire (primary) nodes. Coupling to the volumetric grid requires the wire current to be defined on primary edges. Let the average wire current on the *p-th* primary edge be denoted by $\tilde{I}_p$. Coupling to the volumetric grid is then approximated through the equation (cf. Fig. 9)

$$\varepsilon_o \frac{\partial}{\partial t}\int_{A_{j,p}^e} E_p \, dA_p = \oint_{C_{j,p}^e} \tilde{\mathbf{H}}^{\mathbf{t}} \cdot d\mathbf{l} - \tilde{I}_p \frac{\mathbf{s}_p^h \cdot \mathbf{n}_{j,p}^e}{\left|\mathbf{s}_p^h \cdot \mathbf{n}_{j,p}^e\right|} \quad (2)$$

To ensure stability, the time-averaging scheme introduced in [1] is applied to the time-integration used for Eq. (2). The spatial integration is over the dual face pierced by primary edge, $\mathbf{s}_p^h$. The normal to this face is denoted by $\mathbf{n}_{j,p}^e$, and the face area is denoted by $A_{j,p}^e$. E_p represents the electric field normal to the dual face, while $\tilde{\mathbf{H}}^{\mathbf{t}}$ denotes average magnetic fields on the dual edges enclosing the face. A more detailed discussion of the grid topology can be found in [1].

The vector electric fields at primary nodes, $\mathbf{E}_j^{\mathbf{t}}$, are approximated using a least-squares fit to the face-normal electric fields (E_p). The average electric field projected in the primary edge direction is

$$\tilde{\mathbf{E}}^{\mathbf{t}} \cdot \mathbf{s}_p^h = \frac{1}{2}\left(\mathbf{E}_j^{\mathbf{t}} + \mathbf{E}_k^{\mathbf{t}}\right) \cdot \mathbf{s}_p^h +$$

$$\left[E_p - \frac{1}{2}\left(\mathbf{E}_j^{\mathbf{t}} + \mathbf{E}_k^{\mathbf{t}}\right) \cdot \mathbf{n}_{j,p}^h\right]\left(\mathbf{n}_{j,p}^h \cdot \mathbf{s}_p^h\right) \quad (3)$$

The integral-equation technique is demonstrated by examining scattering by three curved wires in free space. The simulation is performed two times. In the first case, $\nu = 0$ in Eq. (1) is used, whereas in the second case, $\nu = 1$. Because the geometry involves only wires, the results of the two simulations should be identical. A contour plot for the electric-field distribution local to the wires is shown in Fig. 10. A Gaussian pulse is incident normal to the plane containing the wires. The far, back-scattered field comparing the two simulations is shown in Fig. 11. The wires were locally encapsulated in skewed hexahedral elements that were embedded in tetrahedra. The unstructured-grid block was then embedded in a cubical FDTD mesh out to the grid termination using 5-cm cells.

3.2 Partial Differential Equation Thin-Wire Model

Using a partial differential equation (PDE) model, or equivalently, a transmission-line (TL) model, the wire electric current is defined on primary edges, while the voltage (or charge) is defined at primary nodes. This formulation has a more natural correlation with an FDTD or FVTD volumetric grid than the IE method (which defines current at primary nodes). In both models, wires are defined using one-dimensional beam elements.

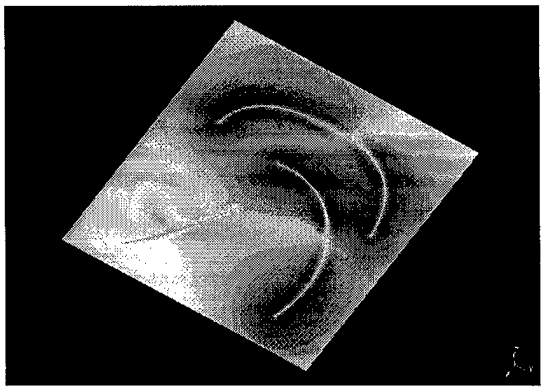

Fig. 10. Scattered electric field surrounding three wires. The wire radius was 2.5 mm and the average edge length was 5 cm. An FDTD grid encloses the unstructured grid.

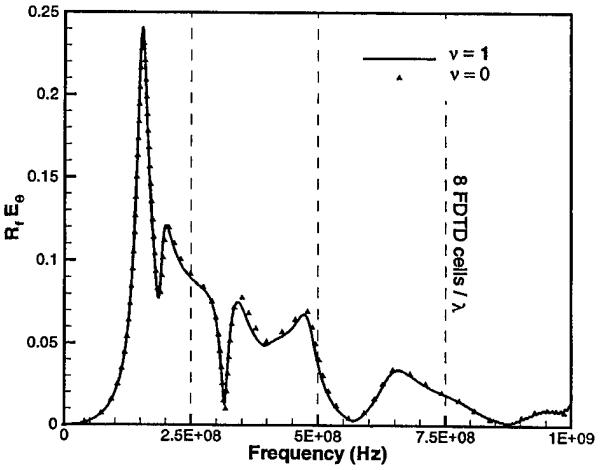

Fig. 11. Normalized, far, back-scattered field from the wire system with feedback on (ν=1), and off (ν=0). R_f denotes distance.

The governing equations along an arbitrary path defined by the spatial variable, l, are the following [cf. 6,7 for an FDTD implementation]:

$$\frac{\partial}{\partial l} I = -C_w \frac{\partial V}{\partial t} \tag{4a}$$

$$\frac{\partial}{\partial l} V = -L_w \frac{\partial I}{\partial t} + \mathbf{E}^{\mathbf{t}} \cdot \mathbf{s} + V^{inc} - I R \tag{4b}$$

I represents current while V denotes voltage. $V = 0$ when the wire terminates on a conductor, whereas $I = 0$ at an open-end termination. The "in-cell" capacitance and inductance are denoted by C_w and L_w, respectively.

With reference to Fig. 8, an explicit algorithm is

$$V_j^{n+1} = V_j^n - \frac{\Delta t_u}{C_{w_j} \left| \mathbf{l}_j \right|} \left(I_p^{n+1/2} \xi_{j,p} - I_k^{n+1/2} \xi_{j,k} \right) \tag{5a}$$

$$I_p^{n+3/2} = \frac{B_p}{A_p} I_p^{n+1/2} - \frac{1}{A_p} \left[\left(V_k^{n+1} - V_j^n \right) - \tilde{\tilde{\mathbf{E}}}^{\mathbf{t}} \cdot \mathbf{s}_p^h - V_p^{inc} \right] \tag{5b}$$

where

$$\xi_{j,p} = \frac{\mathbf{l}_j \cdot \mathbf{s}_p^h}{\left| \mathbf{l}_j \cdot \mathbf{s}_p^h \right|}; \quad \xi_{j,k} = \frac{\mathbf{l}_j \cdot \mathbf{s}_k^h}{\left| \mathbf{l}_j \cdot \mathbf{s}_k^h \right|}$$

$$A_p = \frac{\left| \mathbf{s}_p^h \right| L_{w_p}}{\Delta t_u} + \frac{1}{2} R_p; \quad B_p = \frac{\left| \mathbf{s}_p^h \right| L_{w_p}}{\Delta t_u} - \frac{1}{2} R_p$$

$$C_{w_j} = \frac{2\pi \tilde{\varepsilon}_j}{ln\left(\zeta_j / a\right)}; \quad L_{w_p} = \frac{1}{2} \frac{\left(\tilde{\mu}_k + \tilde{\mu}_j\right)\left(\tilde{\varepsilon}_k + \tilde{\varepsilon}_j\right)}{\left(C_{w_k} + C_{w_j}\right)}$$

V_p^{inc} and R_p denote an impressed voltage source and resistance, respectively, on the *p-th* primary edge. $\tilde{\mu}_j$ and $\tilde{\varepsilon}_j$ denote average permeability and permittivity, respectively, at the *j-th* primary node. a is the wire radius, and Δt_u is the time-step in the unstructured mesh. A superscript, n, denotes time iteration.

ζ_j and $\tilde{\tilde{\mathbf{E}}}^{\mathbf{t}} \cdot \mathbf{s}_p^h$ represent critical quantities that determine the accuracy the of PDE thin-wire method on a random unstructured mesh. ζ_j represents an average distance to the dual nodes that surround the *j-th* primary (wire) node. $\tilde{\tilde{\mathbf{E}}}^{\mathbf{t}} \cdot \mathbf{s}_p^h$ represents an average of the vector electric fields surrounding the endpoints of the *p-th* primary edge, projected onto this edge. Figure 12 shows a two-dimensional representation of the geometry.

ζ_j and $\tilde{\tilde{\mathbf{E}}}^{\mathbf{t}} \cdot \mathbf{s}_p^h$ are computed as follows (cf. Fig. 12).

$$\zeta_j = \frac{1}{m} \sum_i s_{j,i}$$

$$\tilde{\tilde{\mathbf{E}}}^{\mathbf{t}} \cdot \mathbf{s}_p^h = \frac{1}{2} \left(\frac{1}{m} \sum_i \mathbf{E}_{j,i}^{\mathbf{t}} + \frac{1}{n} \sum_i \mathbf{E}_{k,i}^{\mathbf{t}} \right) \cdot \mathbf{s}_p^h$$

where the summations are taken over the valid primary nodes or edges that support the wire node.

The wire current at each time iteration is obtained by solving Eqs. (5a, b). The current is injected onto the volumetric grid in a manner similar to Eq. (2).

For demonstration, the input admittance of a wire-loop antenna defined on a tetrahedral mesh is examined. The loop diameter is 15 cm and the wire diameter (2 a) is 0.5 mm. The loop is modeled on tetrahedral elements with an average edge length of 1.08 cm. The unstructured mesh is embedded in a uniform FDTD mesh with 1-cm cubical elements. A Gaussian-modulated sinusoidal voltage source is impressed on the wire. The planar nodal distribution surrounding the beam elements used to mesh the wire is shown in Fig. 13. The transient driving-point current using the PDE thin-wire algorithm is shown in Fig. 14. A comparison is made with the previous IE thin-wire algorithm for the case $\upsilon = 0$ (no feedback). As seen, the results are virtually identical. The input admittance is shown in Fig. 15.

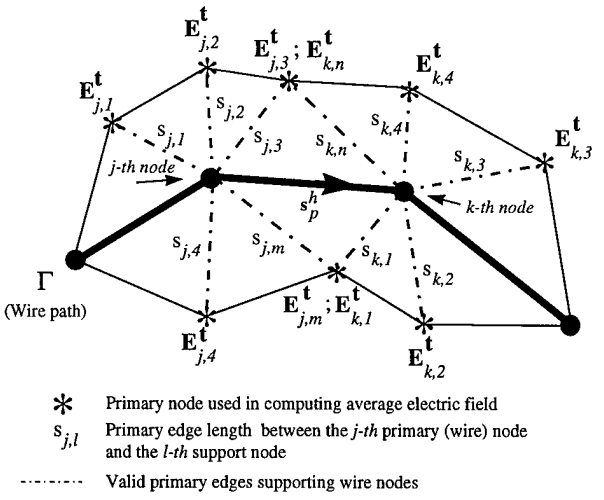

Fig. 12. Primary edges and nodes used in computing average electric fields and edge lengths supporting wire nodes.

4. Sub-Cell Slot Modeling

Several algorithms have been proposed to model narrow apertures on rectangular FDTD grids [5,6,10,12]. However, none of the algorithms have been extended to unstructured grids with non-orthogonal cells. Such an extension is made in this section for the hybrid thin-slot algorithm (HTSA) [5]. The HTSA uses a transient integral equation to model the slot physics.

Similar to the IE thin-wire algorithm described in Section 3.1, the HTSA also uses a field-feedback technique to account for the presence of solid geometry in the neighborhood of the slot. The original algorithm for linear apertures has been shown to be accurate, but long-term stability is dependent on the implementation [10,13,14]. The generalized HTSA presented in this section largely resolves stability issues while permitting slots to follow an arbitrary path in a plane. The requirement that the slot is locally planar is a consequence of applying the equivalence principle [15] in conjunction with the free-space Green's function.

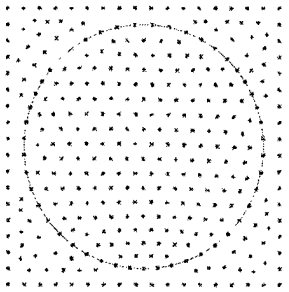

Fig. 13. The nodal distribution in the loop plane of the unstructured grid.

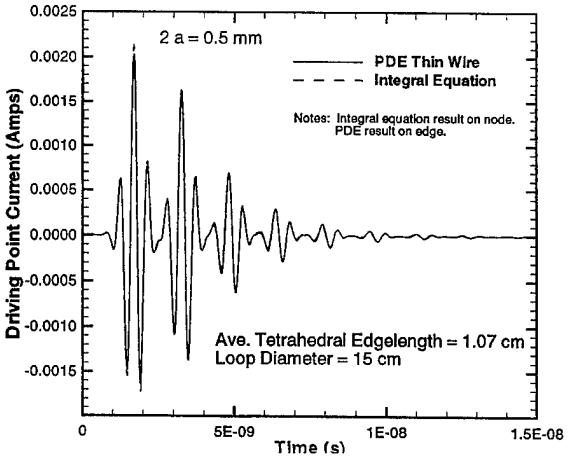

Fig. 14. The loop transient driving-point current.

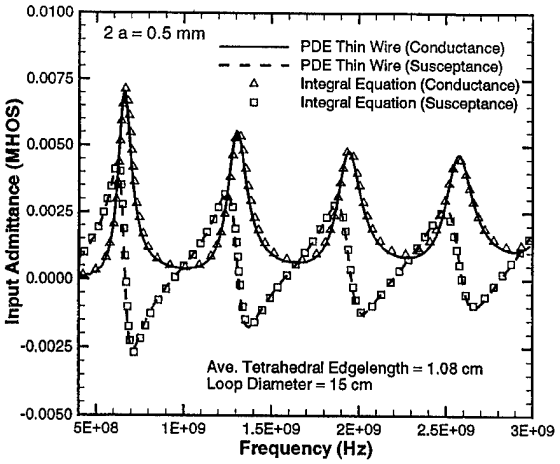

Fig. 15. The loop input admittance.

A slot in a perfectly conducting plane is shown in Fig. 16. Fields are assumed to be incident from both region 1 and region 2. A derivation of an IE for the magnetic current can be found in [10,11]. The HTSA generalizes the standard slot IE by utilizing the total magnetic field from the volumetric grid as a source for the IE. This field includes not only the usual "short-circuit" terms required by the standard IE, but also includes the slot radiation and any additional scattered fields due to finite geometry. The technique is particularly well suited to FDTD, or FVTD formulations that use interleaved grids. The resulting equation is given by [10]

$$\frac{\mu_o}{4}\mathbf{l}\cdot\frac{\partial}{\partial t}\mathbf{H}^{t_1}-\frac{\mu_o}{4}\mathbf{l}\cdot\frac{\partial}{\partial t}\mathbf{H}^{t_2}=$$
$$\frac{1}{c^2}\frac{\partial^2}{\partial t^2}\int_\Gamma dl'\,\mathbf{l}\cdot\mathbf{l}'\,K(l',\tau)\left[G(\mathbf{r},\mathbf{r}';a)-G(\mathbf{r},\mathbf{r}';a_o)\right]-$$
$$\mathbf{l}\cdot\nabla\int_\Gamma dl'\,\nabla_{l'}'\cdot\left[\mathbf{l}'\,K(l',\tau)\right]\left[G(\mathbf{r},\mathbf{r}';a)-G(\mathbf{r},\mathbf{r}';a_o)\right] \quad (6)$$

where $\mathbf{r}\in\Gamma$, K denotes the magnetic current, and $G()$ denotes the free-space Green's function. The equivalent thin-wire radius, a, for the thin slot is $a=(w/4)\exp\left[-\pi d/(2w)\right]$ [16], where w denotes the slot width and d denotes the slot depth. The total magnetic fields in region 1 and region 2 of the slot plane are denoted by $\mathbf{H}^{t_1}$, and $\mathbf{H}^{t_2}$, respectively. The magnetic fields represent average values local to the slot, such that the respective sides of the slot plane are honored in the average. They are computed by averaging over the vector magnetic fields located at the dual nodes that surround appropriate dual faces. a_o is defined to be an average distance from the slot to the surrounding local magnetic field locations (dual node locations). Other parameters are as defined for Eq. (1). Numerical solution details for the IE can be found in [10,11].

Faraday's law is used to apply the magnetic current onto the volumetric grid. Only the primary faces that have a single edge on the slot plane, and only a single slot node, are used with the appended magnetic current (cf. Fig. 16). For the *l-th* face on the *i-th* primary cell,

$$\mu_o\frac{\partial}{\partial t}\int_{A^h_{i,l}}H_l\,dA_i=-\oint_{C^h_{i,l}}\tilde{\mathbf{E}}^t\cdot d\mathbf{l}\pm\frac{K_j}{2}\frac{\mathbf{l}_j\cdot\mathbf{n}^h_{i,l}}{\left|\mathbf{l}_j\cdot\mathbf{n}^h_{i,l}\right|} \quad (7)$$

The "+" sign is for region 1, whereas the "-" sign is for region 2. Note the ½ scaling factor applied to the magnetic current. This is because the slot is defined to lie along primary edges. Thus, the contribution due to the

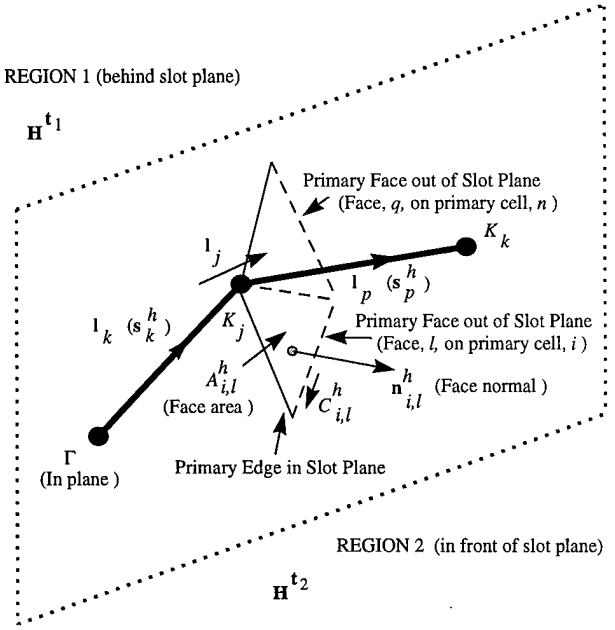

Fig. 16. Arbitrary slot path in a plane.

slot is apportioned to the primary faces that lie "above" and "below" the aperture. This is a distinction relative to previous thin-slot algorithms that assume the aperture falls at the midpoint of the primary edge that passes through the slot. Defining the slot on primary edges enables it to be included in the original solid model and meshed using beam elements. Because beam elements are used for both wires and slots, the nodes associated with the beam elements are given either a slot or wire attribute to activate the appropriate algorithm within *VOLMAX*. Consequently, multiple wires and slots can reside within the same mesh.

The vector magnetic field local to the slot is approximated by forming a least-squares fit to the face-normal magnetic fields. The vector field projected along dual edges is defined similar to Eq. (3) [1]. An example of thin-slot/thin-wire coupling is provided in the following section.

5. EMC/EMI Applications

Electromagnetic compatibility (EMC) and electromagnetic interference (EMI) issues are important in system applications. Effective shielding is often crucial to survivability and/or vulnerability requirements. Two shielding enclosure examples are presented in this section. These examples were previously investigated in [13,14] to examine the accuracy of rectilinear FDTD thin-wire and thin-slot algorithms in simplistic, but realistic geometry. The FDTD simulations were compared to measurements with good agreement over the simulation bandwidth. The geometry studied con-

formed to a rectangular grid. Using rectilinear FDTD on a rotated geometry, however, can lead to significant errors in slot, wire, and cavity resonance locations [10]. In the following, the rectangular shielding enclosures are modeled using a tetrahedral mesh in conjunction with the generalized thin-wire and thin-slot algorithms. This largely removes FDTD geometrical constraints.

The first example is a closed rectangular resonator that is driven by a 50 Ω source/coaxial line. The geometry, with partial mesh, is shown in Fig. 17. A thin-wire was used with a 50 Ω termination at the top of the resonator and a 47 Ω termination at the bottom of the resonator. The diameter of the wire was 0.16 cm. The entire geometry was built as a solid model and automatically meshed with linear tetrahedral elements. Construction time was approximately 15 minutes using a Sun Ultra Sparc computer. Because the geometry represents an interior problem, there was no need to embed the unstructured grid in an FDTD mesh to form the hybrid-grid configuration.

The power delivered by the source (calculated at the 50 Ω impedance) is shown in Fig. 18. The *VOLMAX* simulation used the tetrahedral mesh, with an average edge length of 1.1 cm, in conjunction with the PDE thin-wire algorithm (Section 3.2). Comparison with measured data is made [13]. The power available from the source was 2.5 mW. The agreement is generally good. A slight (< 1%) shift in cavity resonances at approximately 1.4 GHz and 1.5 GHz is seen. It was noted in [13] that minor changes in the wire radius affect all resonance locations. No effort was made in Fig. 18 to "tune" the results; the physical wire diameter of 0.16 cm was used.

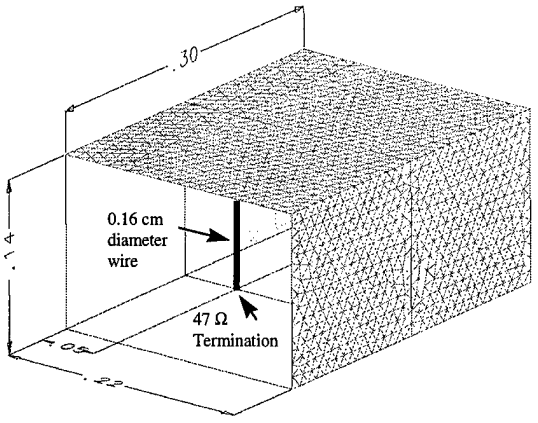

Fig. 17. Closed rectangular shielding enclosure with thin wire. 50 Ω termination at top of wire (not shown). Units in meters unless noted. Tetrahedral meshed.

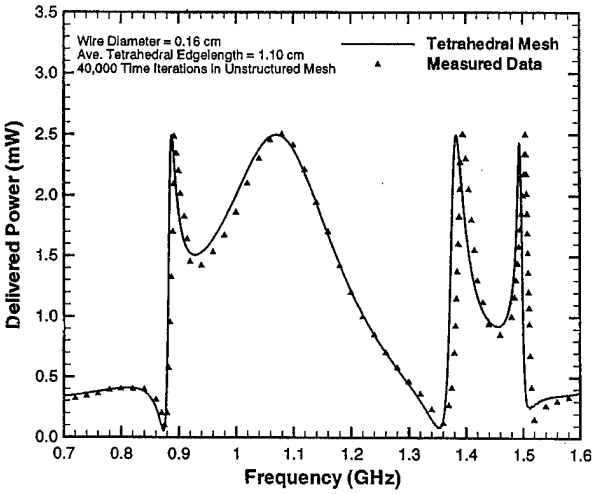

Fig. 18. Power delivered by source for Fig. 17 geometry.

The second example is similar to the first, but adds a narrow slot, with depth, to the shielding enclosure. Because this is now an open geometry, a full hybrid-grid implement is used in *VOLMAX*. The interior of the enclosure is automatically meshed with linear tetrahedral elements, as well as a 1-cell-layer external to the enclosure. To accomplish this simply requires "partitioning" the enclosure geometry out of a slightly (1-cell) larger rectangular container--a task that is easily done within the CAD system. This extra layer of tetrahedral elements enables the wrapper layer to be constructed by *PreVol* (cf. Section 1) for direct interface to a cubical FDTD grid that is used to terminate the overall mesh.

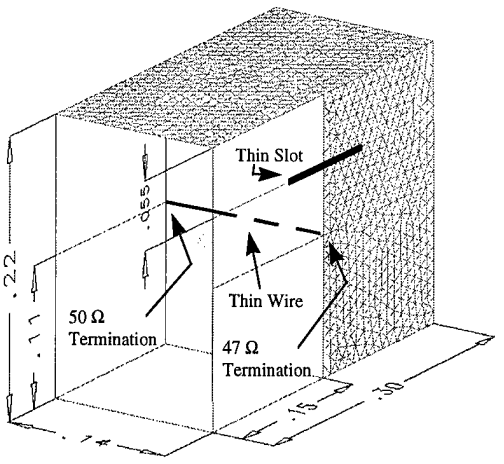

Fig. 19. Enclosure with wire and slot. Wire terminated as in Fig. 17. Slot width, 0.1 cm, slot depth, 0.05 cm, slot length, 12 cm. Wire diameter, 0.16 cm. Units in meters unless noted. Tetrahedral meshed.

The power delivered by the source is shown in Fig. 20. Comparison with measured data is made [14]. The calculation is again made at the 50 Ω load. As in the previous example, there is a slight (< 1%) shift in resonance locations. The PDE thin-wire model (Section 3.2) and the generalized HTSA model (Section 4) were used in conjunction with the tetrahedral mesh. The resonances at approximately 1.13 GHz, 1.26 GHz, and 1.38 GHz are due to the slot. The transient response ran for 35,000 time iterations in the unstructured mesh (5,000 in the structured-grid portion of the hybrid mesh). No indication of instability was observed when using the standard *VOLMAX* time-averaging scheme on the unstructured mesh [1]. Note that the Q of all resonances is well characterized by the simulation for both examples.

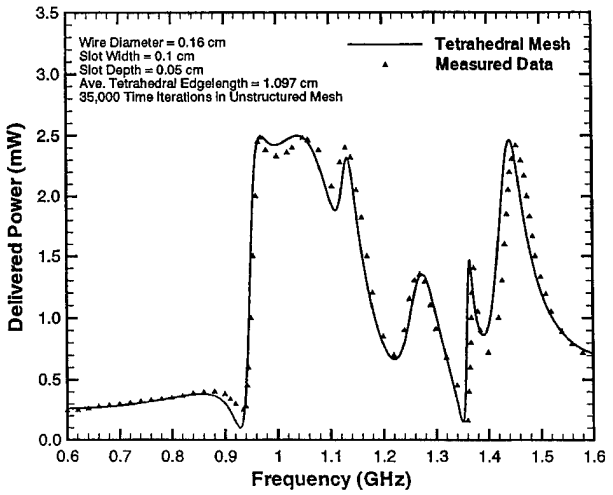

Fig. 20. Power delivered by source for Fig. 19 geometry.

6. Concluding Remarks

VOLMAX is a general-purpose, transient electromagnetic field simulator that operates on hybrid-grid structures. It is coupled to a commercial CAD system that provides advanced solid-modeling, meshing, and post processing. *VOLMAX* has been optimized for shared-memory, multi-processor computer systems (SMP). On a four-processor, Sun Ultra SPARC platform, performance ranges from 0.2 μs/cell-time-step for multi-million element structured grids, to 4 μs/cell-time-step for purely unstructured grids with a few thousand elements. Hybrid-grid problems fall between these limits.

The introduction of sub-cell wire and slot algorithms on unstructured grids significantly extends the application domain. Detailed source modeling, microelectronic packaging, complex aperture coupling and particle-in-cell (PIC) applications are currently being investigated.

Acknowledgment

Sandia is a multiprogram laboratory operated by Sandia Corporation, a Lockheed Martin Company, for the United States Department of Energy under Contract DE-ACO4-94AL85000.

References

1. D.J. Riley and C.D. Turner, "*VOLMAX*: A solid-model-based, transient *vol*umetric *Max*well solver using hybrid grids," *IEEE Antennas Propagat. Mag.*, 39, 1, 1997, pp. 20-33.
2. D.J. Riley and C.D. Turner, "Interfacing unstructured tetrahedron grids to structured-grid FDTD," *IEEE Microwave and Guided Wave Letters*, 5, 9, 1995, pp.284-286.
3. D.J. Riley and C.D. Turner, "Unstructured finite-volume modeling in computational electromagnetics," *11th Annual Review of Progress in Applied Computational Electromagnetics (ACES) Symposium Digest*, 1995, pp.435-444.
4. *I-DEAS Master Series*, Structural Dynamics Research Corporation, Milford, OH, 45150-2789.
5. D.J. Riley and C.D. Turner, "Hybrid thin-slot algorithm for the analysis of narrow apertures in finite-difference time-domain calculations," *IEEE Trans. Antennas Propagat.*, 38, 12, 1990, pp.1943-1950.
6. D.E. Merewether and R. Fisher, *Finite Difference Solution of Maxwell's Equations for EMP Applications*, EMA, Inc., Report: EMA-79-R-4, Albuquerque, NM, April 22, 1980.
7. R. Holland and L. Simpson, "Finite difference analysis of EMP coupling to thin struts and wires," *IEEE Trans. Electromag. Compat.*, 23, 2, 1981.
8. P. Bonnet, X. Ferrieres, F. Issac, F. Paladian, J. Grando, J.C. Alliot, and J. Fontaine, "Numerical modeling of scattering problems using a time domain finite volume method," *J. of Electromag. Waves and Applicat.*, 11, 1997, pp.1165-1189.
9. G.J. Burke, *Numerical Electromagnetics Code—NEC-4*, Report: UCRL-MA-109338, Lawrence Livermore National Laboratory, CA, January, 1992.
10. D.J. Riley and C.D. Turner, *General Implementation of Thin-Slot Algorithms into the Finite-Difference Time-Domain Code, TSAR, Based on a Slot Data File*, Report: SAND91-1061, Sandia National Laboratories, NM, June, 1991.
11. E.K. Reed and C.M. Butler, *Electromagnetic Penetration Through Narrow Slots in Conducting Surfaces and Coupling to Structures on the Shadow Side*, Report: TR-062188-3273F2, Clemson University, SC, July, 1990.
12. J. Gilbert and R. Holland, "Implementation of the thin-slot formalism in the finite-difference EMP code THREDII," *IEEE Trans. Nucl. Sci.*, 28, 1981, pp.4269-4274.
13. M. Li, K.-P. Ma, D.M. Hockanson, J.L. Drewniak, T.H. Hubing, and T.P. Van Doren, "Numerical and experimental corroboration of an FDTD thin-slot model for slot near corners of shielding enclosures," *IEEE Trans. Electromag. Compat.* 39, 3, 1997, pp.225-232.
14. K.-P. Ma, M. Li, J.L. Drewniak, T.H. Hubing, and T.P. Van Doren, "A comparison of FDTD algorithms for subcellular modeling of slots in shielding enclosures," *IEEE Trans. Electromag. Compat.*, 39, 2, 1997, pp. 147-155.
15. R.F. Harrington, Time-Harmonic Electromagnetic Fields, McGraw-Hill, 1961.
16. L.K. Warne and K.C. Chen, "Equivalent antenna radius for narrow slot aperture having depth," *IEEE Trans. Antennas Propagat.*, 37, 1989, pp.824-834.

Report Number (14) SAND--97-2906C
CONF-980322--

Publ. Date (11) 199711

Sponsor Code (18) DOE/[redacted] OR, XF

JC Category (19) UC-900, DOE/ER

DOE